17th Australasian Fluid Mechanics Conference
Auckland, New Zealand
5-9 December 2010

Oro-Pharangeal-Laryngeal Flow Physics

Andrew Pollard and Abdul-Monsif Shinneeb

Department of Mechanical and Materials Engineering
Queen's University, Kingston, ON, K7L 3N6, Canada

Abstract

The oro-pharangeal-laryngeal human airway is a complex geometry and the flow physics within is subjected to and influenced by a variety of different factors that produce jet-like flow, re-circulating flows that are enhanced by curvature, detached flows, and secondary flow. Simulation and experiment are the tools available to the fluid dynamics researchers. Simulation results obtained from direct and large-eddy simulation, and Reynolds-averaged Navier-Stokes and associated models of turbulence are reviewed. Experimental data obtained through the use of flow visualization, hot-wire anemometry and particle image velocimetry are also reviewed. A comparison of data obtained from the application of these tools reveals many inconsistencies, which are explored in this paper. While much progress has been made to understand some of the flow physics of the flow in the human airway, we continue to uncover new and significant fluid dynamic behaviour. The paper also suggests options for future research directions.

Introduction

The oro-pharangeal-laryngeal (OPL) human airway, defined here to include only the oral cavity, the non-nasal pharynx, the larynx and trachea, is a complex geometry. Breathing through the mouth is more efficient than breathing through the nasal orifice because the flow resistance is lower, thus greater volumes of oxygen/carbon dioxide can be exchanged during the inhalation-exhalation breathing cycle. Reynolds numbers (Re) within the human airway can be wide ($650 < Re < 13{,}000$, see [1]) depending on inhalation flow rate and location in the airway. Reynolds number is defined here as $Re = U_B\sqrt{A}/\nu$ where U_B is the local bulk velocity at the airway location with local cross-sectional area A. Note that the Reynolds number implies laminar-like through transition and into the fully turbulent flow range.

The fluid mechanics in the nasal passages is complicated by the turbinates which maximise exposure of the delicate tissues to the incoming air, thereby enabling the air to be raised in temperature, humidified, and cleansed prior to exiting the nasal-pharynx region. Then the air passes over the epiglottis and through the larynx before entering the trachea and eventually the lungs. The peak Reynolds number in the nasal passages based on hydraulic diameter is of order 1000 [2]. While this suggests possible dominance of the inertial forces, there are regions in the turbinates where the flow is much slower so that diffusion controlled mass transfer takes place to the olfactory glands. In this work, the flow in the nasal passages is ignored; interested readers may consult that literature (see for example [2, 3, 4, 5, 6, 7]).

The actual geometry of the human airway is highly variable; it is patient-specific and age-dependent. Heenan et al. [8] considered two realistic geometries, derived from magnetic resonance imaging (MRI), to explore deposition of aerosol in the airway (see also [**?**]). These two geometries were referred to as 'large mouth/small nose' and 'small mouth/large nose' are examples of the high variability that may be encountered. Further, the presence of soft tissues (e.g. the tongue) complicates the geometry because it is difficult to preserve the shape of these tissues postmortem. In fact, these real geometry were from healthy subjects; in the case of diseased airways, these geometries may be even more complex. Although it is recognised that specific features of airway geometry have a major influence on the flow structure, the global flow behaviour can be inferred quite adequately using idealised models [9].

Here, the idealised airway geometry is used. This geometry contains all the basic physiological elements found in the actual airway. Further details will be provided below. In this paper, the interplay between simulation and experiment is considered and attention is drawn to the strengths and weaknesses associated with their application and the care required in interpreting those data that result. Moreover, the flow in the airway is essentially a collection of basic flows that engineers are somewhat familiar with; flows of backward and forward facing steps, flow in curved ducts, and jet flows.

The paper is laid out as follows. The idealised geometry is described and the interesting fluid dynamic regions are highlighted. The experimental methods that have been employed to investigate the flow in the airway are described followed by the various computational options. This is then followed by presentation and discussion of results, with emphasis on weaknesses in those data obtained from both experiment and simulation. Some new data obtained from full field PIV is also presented that enables some of these weaknesses to be addressed. Finally, the paper concludes with some suggestions for future work.

The Idealised Geometry

As indicated earlier, the geometry of the oro-pharangeal-laryngeal (OPL) or extra-thoracic airway (ETA) is complex and varies largely from person to person. It varies too with with inhalation, physical fitness, and disease states. For these reasons, it is found that creating an idealised model that represents averaged-extra-thoracic airways geometry of healthy individuals is more practical. This enables direct comparison between different experimental and computational data obtained in the same geometry, and is also suitable for CFD studies because extremely high grid resolutions are not needed at the walls to resolve all of the small airway irregularities as in realistic models. Figures 1 and 2 show the human respiratory tract and a sagittal view of the idealised OPL/ETA model, respectively. The

idealised geometry is built up of simple geometric shapes that possess all the basic anatomical features of real OPL/ETA geometry. The main components of the OPL/ETA model include the oral cavity (mouth), the pharynx, the larynx, and part of the trachea. Note that the nasal cavity is not included in the model because it is assumed to be blocked off during aerosol drug delivery. This design was developed based on information from MRI and CT scans, direct observation of living subjects and data in the archival literature. The rationale behind the geometry and choice of dimensions are fully described in [10].

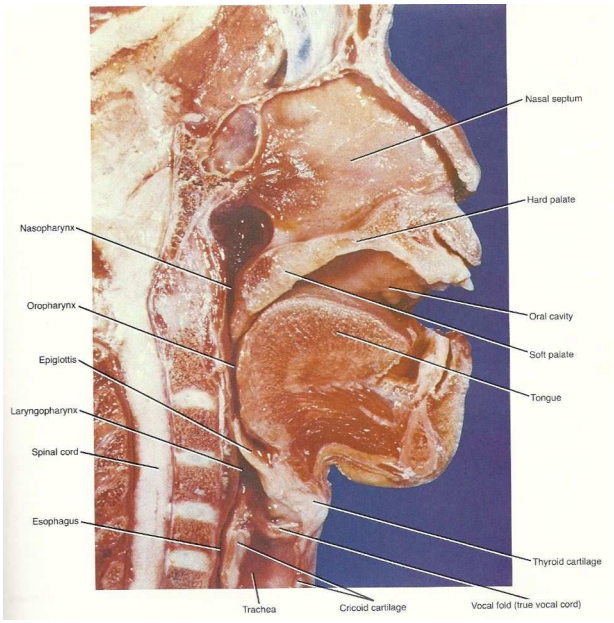

Figure 1: The human oro-pharangeal-laryngeal duct. From: Principals of Anatomy and Physiology, Tortora and Anagnostakos, Harper and Row, 1984

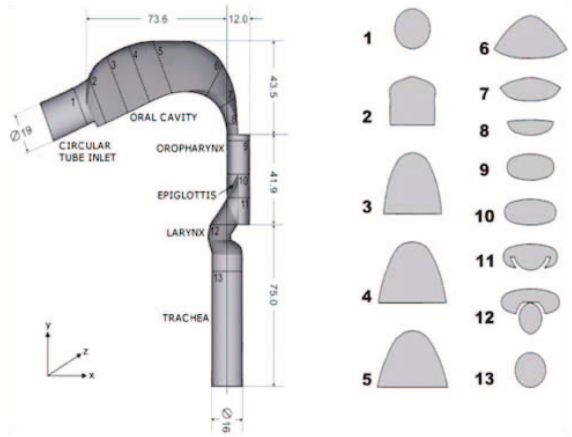

Figure 2: Dimensions of the idealised OPL/ETA geometry and cross-sectional views of the airway passage.

The cross-sectional shape of the idealised geometry shown in Figure 2 also presents some interesting fluid dynamic challenges. The cross-sectional geometry begins with a round pipe (represents an idealised inhalation device) and then expands into an almost 'slice-of-bread' shaped cross-section before it evolves into a half-ellipsoid, then to a full ellipsoid just before the epiglottis and finally reverting again to a round pipe that represents the trachea. Figure 3 displays a sagittal cross-section of the idealised OPL/ETA model and highlights various fluid-dynamically interesting regions which are: (a, b) recirculation behind the teeth; (c) destabilising flow curvature; (d) stabilising flow curvature; (e) flow separation distal to the nasal pharynx; (f) recirculation around the epiglottis; (g) flow acceleration around the epiglottis; (h) the laryngeal jet; and, (i) recirculation distal to the larynx.

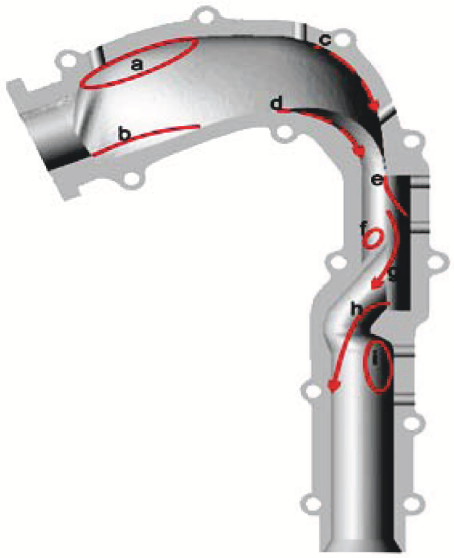

Figure 3: A sagittal cross-section of an idealised OPL/ETA model. The geometry may be decomposed into simple geometric shapes and the red lines highlight regions that are of fluid dynamic interest.

Experimental Interrogation Options

Experiments that employ the idealised geometry can use one of two approaches: invasive and non-invasive methods. In each case, the choice must be made to consider if the flow is to be treated as a constant inhalation rate or time dependent; in the latter case, a pulmonary wave form may be introduced (see [16]), which enhances flow instabilities and flow features (unpublished work in author's lab.). These effects are not generally known, but it may be assumed they are functions of the local Reynolds number, which of course will then vary both in space and time.

Invasive probe insertion may be of two types: introduction of either an optical boroscope or hot wires (see [1]). In the case of a boroscope, this may be used for flow visualisation studies [1] or to be the optical 'collector' for particle image velocimetry measurements [8]. In either case, the introduction of physical probes in a confined space may alter the flow (and pressure) in the immediate region of the probe [11]. Alternatively, non-

invasive methods can be used, but this requires the development of an optically clear geometry that affords direct visual access to the interior cavity. Typically, this is accomplished using a silicone material that is cast around a rapid prototyped core, which is flushed from the cavity upon curing of the silicone. Examples of these measurement options are provided in Figure 4. In Figure 4(c) the 7 planes indicate measurement planes, reference to which will be made throughout this paper.

Flow Visualisation

The flow in the airway is highly three dimensional and many regions of flow reversal both in the mean flow direction and the transverse-sagittal plane. For example, flow visualisation in the transverse-sagittal plane at location 1 (see Fig. 4c) is shown in Fig. 5. This image indicates the highly distorted flow field (view is from the throat towards the mouth opening) that displays regions of significant lateral strain and cross-stream recirculation in the corners of the oral cavity.

Hot-Wire Anemometry (HWA)

Hot-wire anemometry is unsuitable for use in turbulent flow fields that possess velocities that depart significantly from being unidirectional. The hot-wire anemometer requires careful calibration for regions of low velocity and must also account for thermal conductivity of the wall material, which can distort the thermal boundary layer around the wire. These are not trivial issues [12], especially inside the complex airway model considered here. As with any experiment, measurement errors abound. In the case of cross wires, spatial resolution (especially between the wires) and spatial averaging along the wires (in regions of significant velocity gradients) will affect the accuracy of the results. Recent advances in nano-technology enable the spatial resolution issues to be addressed [13]. An advantage of hot-wire anemometry is the temporal resolution of the signals which is in the kHz range.

Particle Image Velocimetry (PIV)

Optical methods that have been applied to the flow in the airway suffer from limited temporal resolution (typically below 50 Hz, although current technology enables time-resolved data to be obtained). Two approaches have been used: an opaque model where internal interrogation of the sagittal plane was achieved using a boroscope (see Figure 4a and [8]) and the use of an optically clear model that dispenses with the narrow field-of-view boroscope approach, (see [14] and herein).

Magnetic Resonance Imaging (MRI)

Magnetic resonance imaging (MRI) is commonly used in the medical field but rarely in experimental fluid dynamics. Elkins et al. [15] applied MRI to the internal serpentine passage of a gas turbine blade at Reynolds numbers between 10,000 and 15,000 based on the hydraulic diameter. As MRI depends on phase resolution between the MR frequency signal and the fluid motion, the turbulence intensities that can be resolved are relatively low.

Computational Simulation/Modeling Options

The relatively low Reynolds numbers of the flow inside the airway suggest that it is ideally suited to the application of direct numerical simulation (DNS). While we have algorithms to solve Navier-Stokes (N-S) equations, we impose a significant requirement from DNS: the results must be extraordinarily accurate. Flows associated with simple geometries, e.g. channels, pipes, jets, wakes, and mixing layers, are readily handled by DNS. However, the introduction of complex geometries introduces both grid structure issues as well as errors associated with discretisation of the N-S equations on these grids. There have been many approaches to handle complex geometries using DNS. Examples include Seidl et al. [16] who considered a finite volume method applied to turbulent flow over a sphere; Karniadakis [17] who considered both internal and external turbulent flow using a spectral finite element method; Hicken et al. [18] who developed a conservative collocated method for unstructured meshes and applied the method to simple channel flow; Hicken et al. [18] also demonstrated conservation of momentum and energy up to second order; Subbareddy & Candler [19] considered conservation of momentum and energy on unstructured grids and for compressible flow that gave spectral-like resolution for compressible isotropic turbulence. Mittal & Iaccarino [20] review the immersed boundary method that has been applied to both internal and external turbulent flows with good success. It is of interest to note that the idea of immersed boundaries is not new (see [21, 22]), although DNS was not considered.

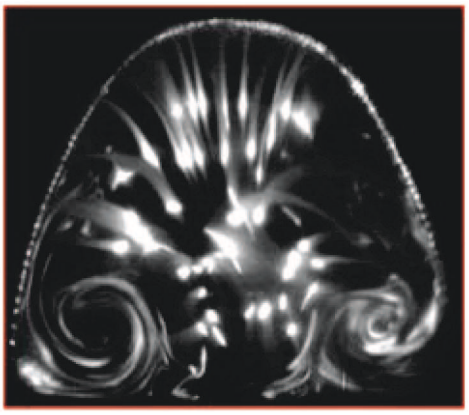

Figure 5: Smoke-wire visualisation at section 1 (see Fig. 4c). The secondary flows in the lower portion of the mouth are visible.

More recently, the lattice-Boltzmann method (LBM) (see for example [23]) and discontinuous Galerkin method (see [24, 25]) have been developed. In our group, Bespalko [26] and Bespalko et al. [27] applied LBM to turbulent channel flow as a precursor test case for application to complex geometries. Ball et al. [28] considered the flow in the human airway using LBM. To perform DNS of any flow, the Kolmogorov length scale determines the resolution requirements. For flow in the human airway at the 10 litre per minute inhalation rate, the Kolmogorov length scale $\eta = (\nu^3/\varepsilon)^{1/4}$ ranges from 0.35 mm to 5.8 mm (where we have assumed $\varepsilon \sim k$), which required a grid resolution of 0.086 mm or $\sim$144 million "control volumes". The LBM must use a uniform cubic grid, so the smallest length scale determines the simulation resolution requirements. The simulation required $\sim$1.5 million time steps and produced over 1 terabyte of data.

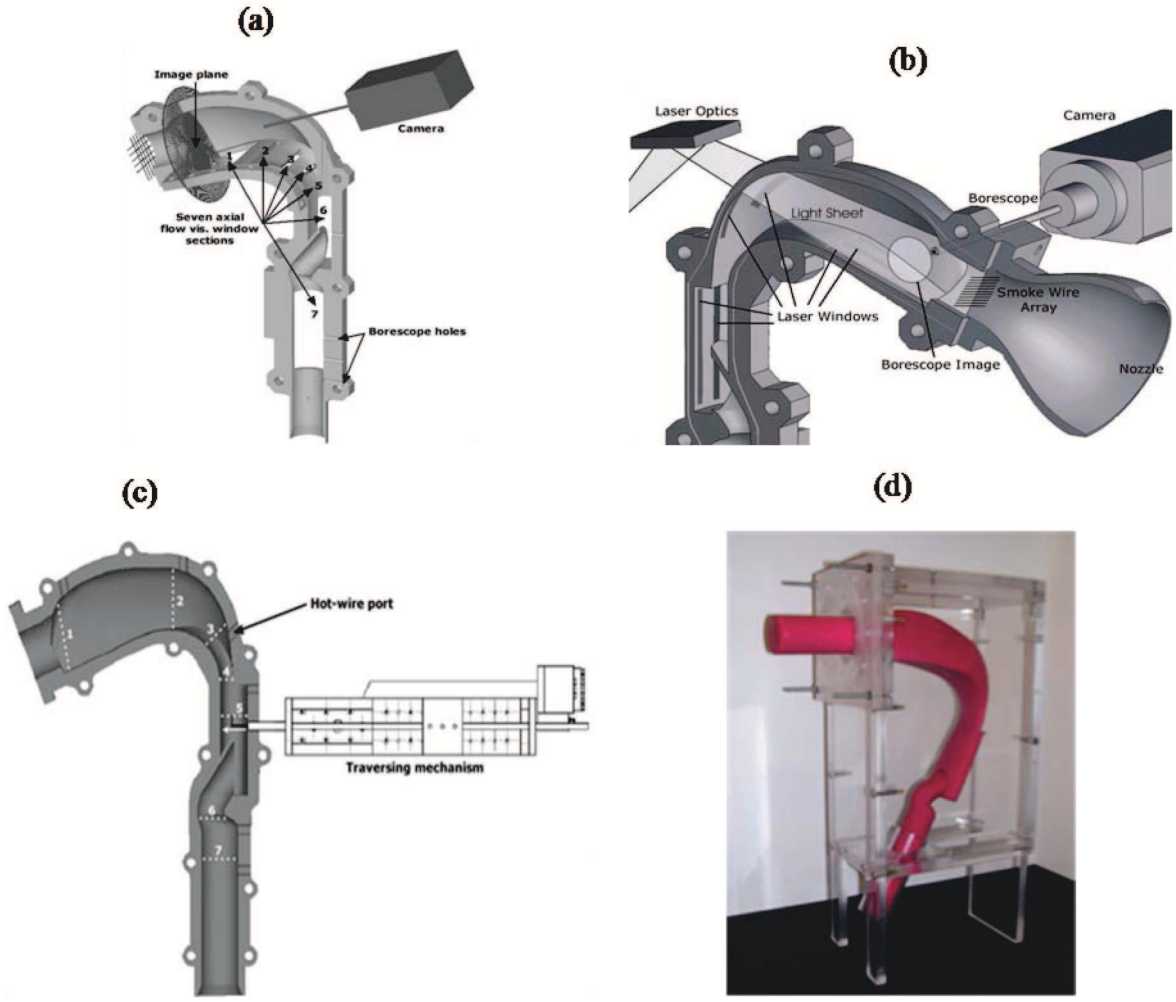

Figure 4: Illustration of invasive and non-invasive experimental methods for studying idealised OPL/ETA; (a) Flow visualisation setup where numbers are measurement planes, (b) Flow visualisation and PIV measurements using boroscope, (c) Hot wire arrangement, and (d) Silicone model before removal of rapid prototyped core (coloured red). Note that in (a), (b), and (c), only a sagittal cross-section is shown.

Wei and Pollard [29] applied the discontinuous Galerkin method (DGM) to compressible flow in channels under the effects of pressure gradients, and considered the effects of Mach number [30]. DGM is admirably suited to handle near wall, pressure gradient, and compressibility effects within a DNS framework and is also ideally suited to parallel computer implementation. It has not yet been applied to the OPL/ETA flow.

LES has been recently employed by Kleinstreuer & Zhang [9] applied to the idealised geometry. However, LES does not appear to provide any significant advantages to well-resolved RANS simulations, at least for the mean flow. There have been a variety of attempts to use RANS (see [31] for current state-of-the-art); however, the use of RANS while computationally appealing, requires the use of models of turbulence that are not 'tuned' to the low Reynolds number range found in the OPL/ETA. We have begun to address this issue in a separate study of *a-priori* and *a-posteriori* testing of RANS using both LES and DNS, [35].

Presentation and Discussion of Some Experimental and Simulation Results

Figure 6 presents results from a mixture of computational approaches that have been applied to the modelled OPL/ETA. A comparison between experimental (single and X hot wires) and computational (RANS and LBM) results are shown in Figures 6(a) and 6(b) at 10 and 15 l/min, respectively. In these plots, the vertical axis represents the value of K normalised by the local bulk mean velocity U_B and the horizontal axis represents the vertical distance y normalised by the square-root of the local cross-sectional area A. Here K is defined by: $K = \sqrt{U^2+V^2+W^2}$, where U, V, and W represent the mean velocity components. The data in these figures were taken at station 2, the location of which is shown in Figure 4(c). Figure 6(a) demonstrates the consistency between the two sets of

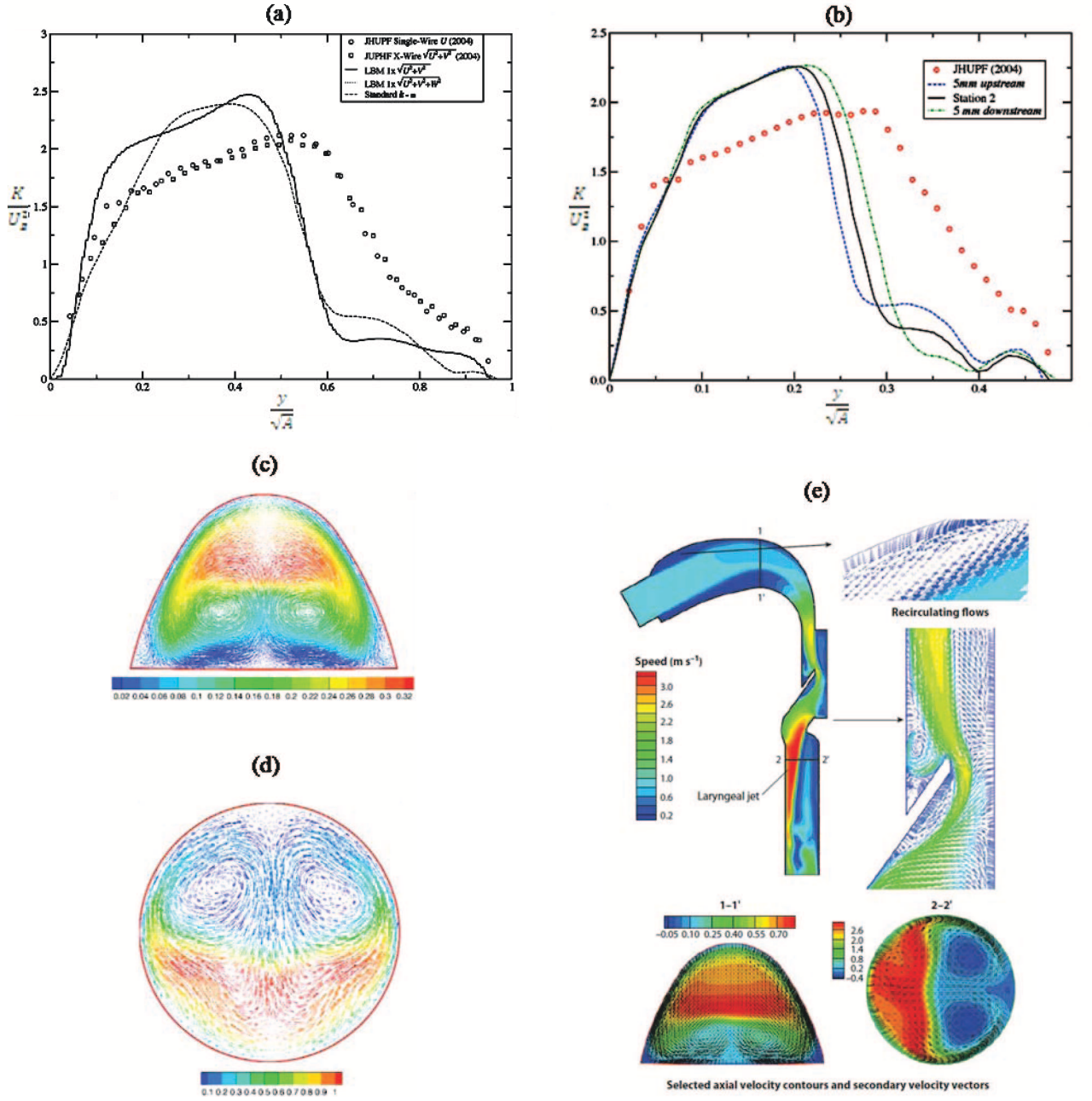

Figure 6: Illustration of previous experimental and computational results: (a,b) variation of K/U_B^2 results with $y/\sqrt{A}$ obtained by HWA and RANS ($k-\omega$) at station 2 for 10 l/min and 15 l/min, respectively; (c,d) vector plots obtained by RANS simulation [31] at stations 2 and 7 (shown in Figure 4c); and (e) LES simulation in the same OPL/ETA model taken from [9]. Note that there is little apparent difference between the RANS (c,d) and LES (e) simulations.

experimental data. Figure 6(a) also indicates the differences between calculations obtained using RANS and LBM. We have explored the differences between the simulations and the experiments; as an example, Figure 6(b) presents the results from possible positioning errors of the hot wires relative to the stated location at station 2. It is clear that this is probably not the cause for the differences observed. The flow field obtained from the simulations at station 2 shown in Figure 6(c) indicates significant cross-flow in the sagittal plane, which casts some doubt as to the ability of the hot-wire anemometry to measure the actual flow field. The flow visualisation indicates that at station 2 there is significant helical motion and transverse movement in the $y/\sqrt{A} > 0.3$ region, which likely influences the experimental data in ways we continue to explore using PIV, see below. The general agreement between simulation results from the DNS-LBM and some RANS turbulence models suggests that RANS ($k-\omega$ in particular) may be a useful tool for exploratory investigations of airway flow in, for example, specific real geometries prior to medically-proposed surgical intervention. The RANS result of Ball et al. [31] depicting the flow in the trachea (station 7 in Figure 4(c) is shown in Figure 6(d). It reveals a non-uniform and vortical velocity distribution in the treachea. Thus, those who wish to model flow in the lungs should be cautioned not to assume a pipe-flow type velocity distribution as inlet conditions to their simulations. The LES results of Kleinstreuer and Zhang [9] shown in Figure 6(e) confirm the finding of Ball et al. [31].

Recent Work

A major limitation to earlier experimental work has been the intrusive and/or point-wise nature of the measurement techniques. Recent advances in optically transparent materials have facilitated the construction of complex flow passages such as the human airway (see Figure 4d). This progress enabled the use of the particle image velocimetry (PIV) technique in complex geometries by using a working fluid with a refractive index that matched that of the model material. The major weakness of the PIV may be the relatively crude temporal resolution of the data (temporal-resolved PIV is currently available in the market). However, this could be advantageous when uncorrelated data are needed for statistical study of the flow structures (see for example [14]).

A series of experiments were carried out in the OPL/ETA model using the PIV at a flow rate of 10 *l/min*. The purpose of this study is to gain more insight into the dynamics of the vortical structures in the OPL/ETA flow. Four fields-of-view (FOV1 to FOV4) were positioned on the sagittal plane as illustrated in Figure 7(a) where the measurements focused on the pharynx to the trachea region. This region was determined in earlier studies to be in poor agreement with experimental results (see for example [28, 31]). Figure 7(b) shows the mean velocity fields calculated from 2000 image pairs that were acquired at each location at a framing rate of 2 Hz. Both the horizontal x and vertical y axes are normalised by the inlet nozzle diameter D. Note that only some rows of vectors are shown to avoid cluttering. In this study (see [36]), PIV data were first analysed using the proper orthogonal decomposition (POD) technique to identify the main energy-containing structures. Using only a few POD modes, the velocity fields were reconstructed which recovered about 60% of the turbulent kinetic energy. These reconstructed

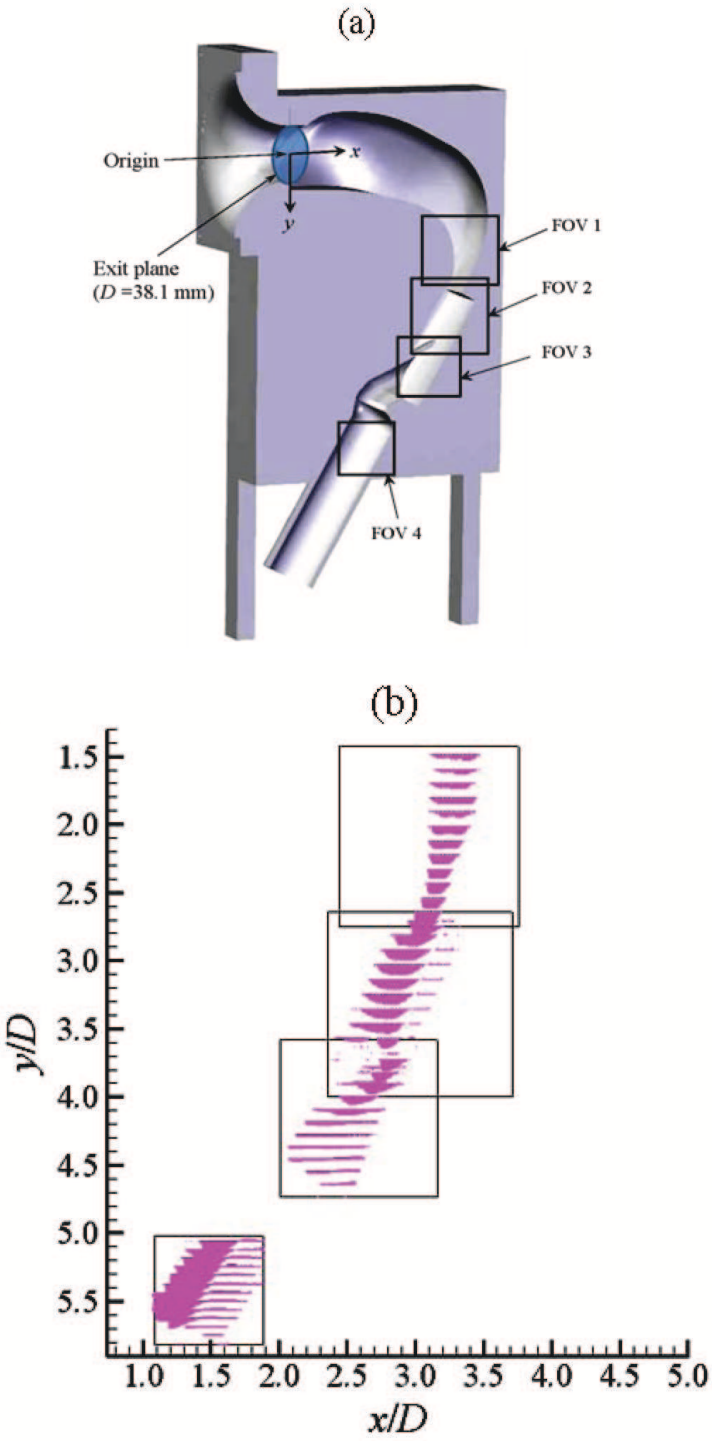

Figure 7: (a) A sagittal cross-section of the OPL/ETA model showing the coordinate system and the position of four fields-of-view (FOV), and (b) the mean velocity fields corresponding to FOV1 to FOV4 in (a) obtained by averaging 2000 instantaneous fields.

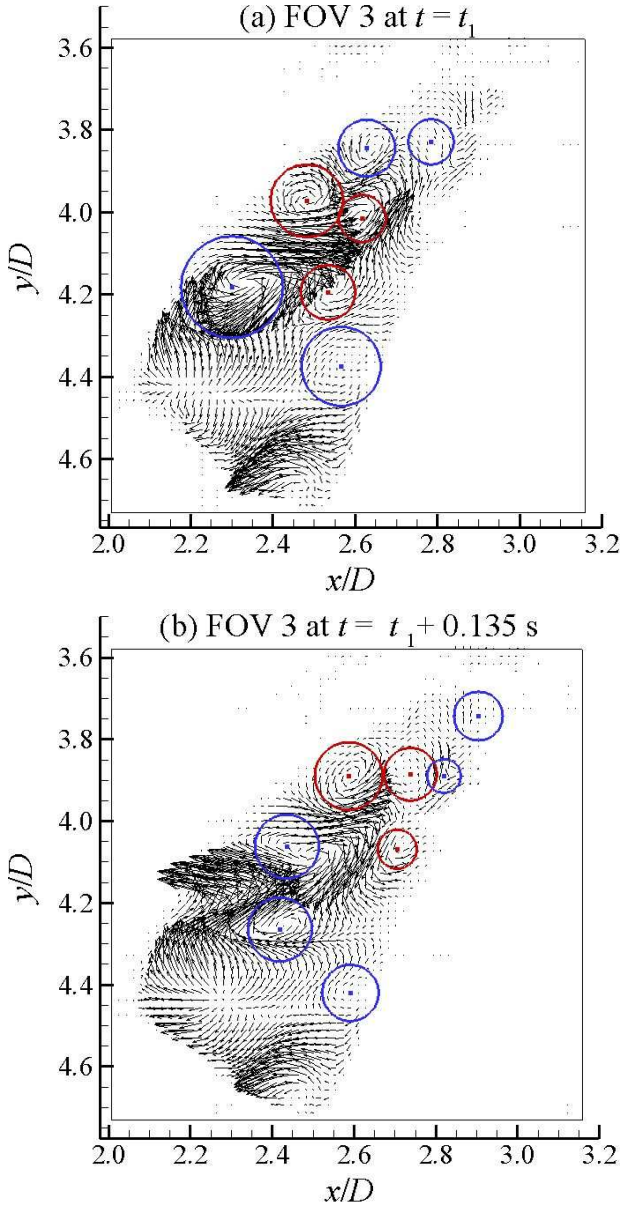

Figure 8: POD-reconstructed fluctuation velocity fields. (a) and (b) represent the flow field in the pharynx region (FOV-3). The lack of vectors in region $3.6 < Y/D < 4.0$ and $2.1 < X/D < 2.7$ indicate the location of the epiglottis. Data taken at time t_1 and t_1 + 0.135 s. Blue and red circles represent clockwise and counter-clockwise rotating structures, respectively.

velocity fields were used as a basis to search for vortical structures using the vortex identification algorithm of Agrawal & Prasad [32]. This algorithm is based on the concept of using closed streamlines to identify vortices. This technique involves searching the POD-reconstructed field for circular streamlines by monitoring the change in direction of the measured velocity vectors along expanding circular paths surrounding candidate vortex centres. The largest such path for which the change in

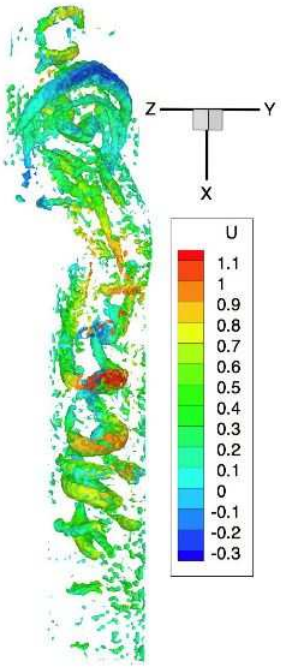

Figure 9: Lattice Boltzmann data, 10 litres per min. inhalation rate, Q-value, coloured by velocity. Note the horseshoe-type vortex around the epiglottis and the complex vortex structure distal to the epiglottis, data from [31]

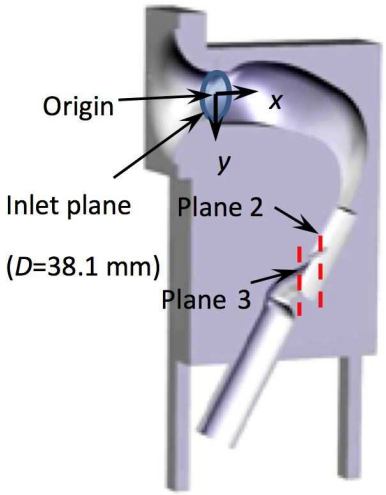

Figure 10: Geometry of the idealized OPL/ETA model. The red lines represent the position of y-z planes. These are located just upstream of and distal to the entrance to the epiglottis (plane 2 and plane 3 respectively).

direction is monotonic for 75% of the vectors defines the size of the vortex. The circulation of a structure is then calculated by integrating along its outermost path. In discrete data, it is calculated by integrating along a polygon path. Figures 8(a) and 8(b) presents selected examples of POD-reconstructed velocity fluctuation fields in the pharynx region. These fields were acquired

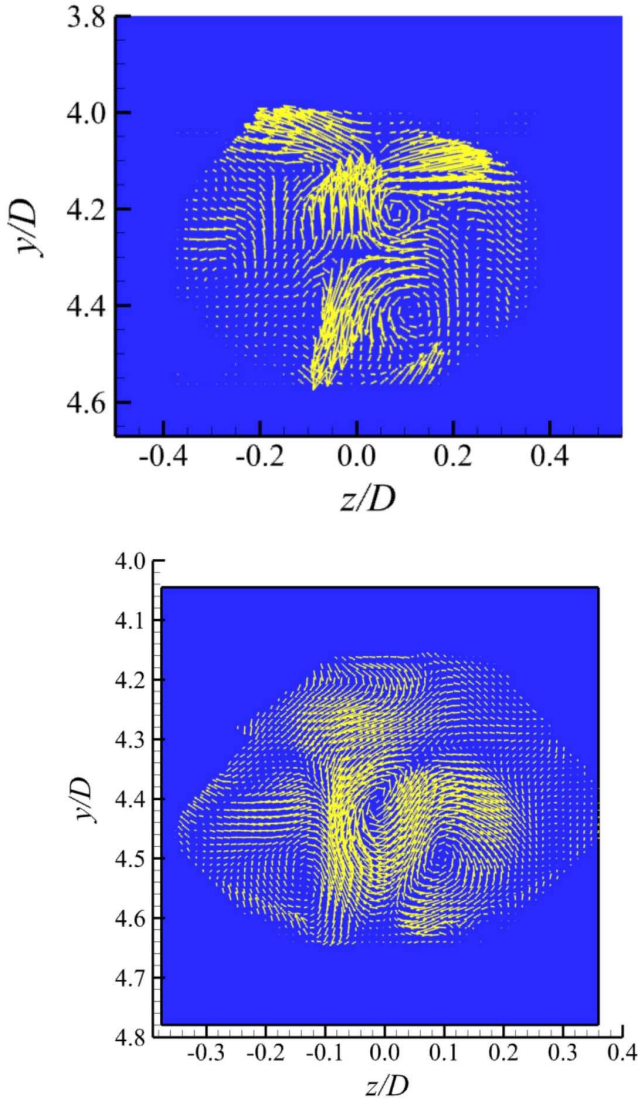

Figure 11: Mean velocity fields in the epiglottal region. Top figure from plane 2; lower figure from plane 3.

at a sampling rate of 7.4 Hz (0.135 s). Red and blue circles represent positive (counter-clockwise) and negative (clockwise) rotating structures, respectively.

A region of flow that we have found particularly interesting is that around the epiglottis. To indicate the richness of the flow in this region, figure 9 flow structures that have been educed from our DNS-LBM simulations. This figure displays surfaces of Q-criterion coloured by velocity. At the top of the figure, the horseshoe-like vortex, coloured blue, indicates a standing vortex anchored around the epiglottis. There is also apparent in that general vicinity, are structures that have been transported from upstream. All these influence the flow entering the epiglottis, attention to which will be shortly addressed. Distal to the epiglottis entrance, the flow structure further develops and is influenced by the strong curvature imposed by the larynx before entering the trachea and transported downstream to the first bronchus.

Figure 10 indicates two planes where PIV data have been recently obtained. The epiglottis is somewhat like a Bourda mouthpiece, except is this case the entrance flow is complicated by upstream influences derived from the oro-pharynx and the fluid enters the mouthpiece obliquely. The data provided in Figures indicate the mean velocity vectors in a y-z plane and Figure V_{rms} respectively. These data indicate the complex, asymmetric and anisotropic feature of the flow in this region. This complexity eventually gives rise to flow symmetry around the sagittal plane in the trachea and asymmetry in the anterior-posterior plane of the trachea noted above (see Figure 6).

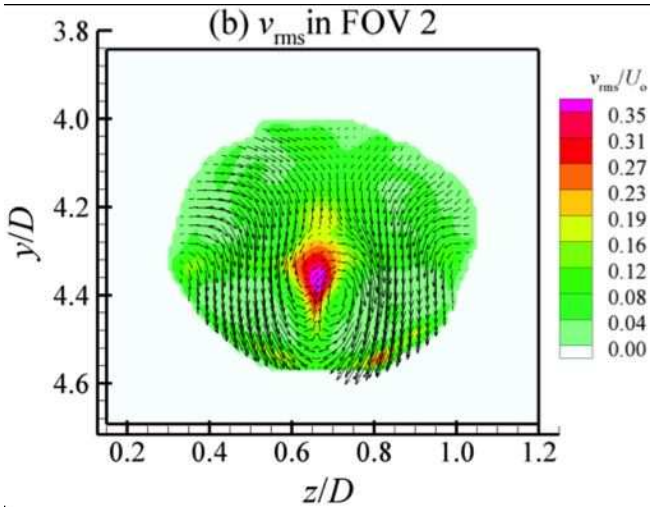

Figure 12: Contour plot of V_{rms} across Plane 2. Velocities normalized by the inlet velocity Uo and locations by the nozzle diameter D. Vectors are the mean flow in the y-z plane. Note the complex secondary mean flow and the peak in *rms*

Summary and Future Prospects

The progress made to understand the flow inside the human airway using evidence gathered from experimental and computational methods has been reviewed. Recent advances in PIV and novel computational approaches to DNS and LES are expected to greatly assist future explorations of this fascinating flow.

The flow physics inside the human airway remains a rich landscape for research. The modelled human airway considered here for the most part was that of a healthy adult; however, the oral pathway geometry may be severely altered by myriad pathological and anatomical variations that could severely influence the flow physics. An example is airway constriction due to adenotonsillar hypertrophy (enlarged adenoid/tonsil), which could introduce higher local Reynolds numbers or because of craniofacial anomalies that will impose asymmetric geometry and therefore possible severe three dimensional unsteady flow behaviour. Additionally, while each human subject has the basic upper airway components considered here, their geometric scales can vary considerably. For example, there is the ”small-mouth/large nose” or conversely the large mouth/small nose” variation so that if nasal flow is introduced including the

changes in the oral pathway entrance condition (lips are slightly pursed for example) the nasal pharyngeal flow will act as a wall-jet with co-flow imposed in the outer region (from the oral portion of the inhalation stream). Sleep apnea is a common problem and obstructive apnea in particular; it occurs due to a severe relaxation in the pharangeal flap or uvula. A sufferer typically uses a positive airway pressure device (mask or nasal "buds") which forces air into the oro-nasal passages to keep the airway open; recent CFD and imaging and future research options may be found in De Backer *et al*.[34]

Acknowledgements

This paper has relied heavily on the work of former students and PDF's in the Computational and Experimental Fluid Dynamics Laboratory at Queen's University. We wish to acknowledge their tremendous contributions. In particular, Dr. Tony Heenan, Professor Mesbah Uddin, Mr. Christopher Ball, and Mr. Andrew Johnstone. Our work was funded from various grants under the auspices of the Natural Science and Engineering Research Council (NSERC) of Canada.

References

[1] Johnstone, A., Uddin, M., Pollard, A., Heenan, A. and Finlay, W.H., The flow inside an idealised form of the human extra-thoracic airway, *Expts in Fluids*, **37**, 2004, 673-689.

[2] Doorly, D.J., Taylor, D.J., Gambaruto, A.M., Schroter, R.C. and Tolley, N., Nasal architecture: form and flow, *Trans. R. Soc. A Math. Phys. Eng. Sci.*, **366(1879)**, 2008, 3225-3246.

[3] Doorly, D.J., Taylor, D.J. and Schroter, R.C., Mechanics of airflow in the human nasal airways, *Respir. Physiol. & Neurobiol.*, **163(1-3)**, 2008, 100-110.

[4] Shi, H., Kleinstreuer, C. and Zhang, Z., Laminar airflow and nanoparticle or vapor deposition in a human nasal cavity model, *J. Biomech. Eng. Trans. ASME*, **128**, 2006, 697-706.

[5] Xi, J.X. and Longest, P.W., Numerical predictions of submicrometer aerosol deposition in the nasal cavity using a novel drift flux approach, *Int. J. Heat Mass Transf.*, **51**, 2008, 5562-5577.

[6] Schroeter, D., Kimbell, J.S. and Asgharian, B., Analysis of particle deposition in the turbinate and olfactory regions using a human nasal computational fluid dynamics model, *J. Aerosol Med. Depos. Clear. Effects Lung*, **19(3)**, 2006, 301-313.

[7] Zamankhan, P., Ahmadi, G., Wang, Z., Hopke, P.K., Cheng, Y.-S., Su, W.C. and Leonard., D., Airflow and deposition of nano-particles in a human nasal cavity, *Aerosol Sci. Technol.*, **40(6)**, 2006, 463-476.

[8] Heenan, A.F., Matida, E., Pollard, A. and Finlay, W., Experimental measurements and computational modelling of the flow field in an idealised extra-thoracic airway, *Expts. Fluids*, **35**, 2003, 70-84.

[9] Kleinstreuer, C. and Zhang, Z., Airflow and Particle Transport in the Human Respiratory System, *Annu. Rev. Fluid Mech.*, **42**, 2010, 301-334.

[10] Stapleton, K.W., Guentsch, E., Hoskinson, M.K. and Finlay, W.H., On the suitability of $k-\varepsilon$ turbulence modeling for aerosol deposition in the mouth and throat: a comparison with experiment, *J. Aerosol Sci*, **31**, 2000, 739-749.

[11] Tropea, C., Yarin, A.L. and Foss, J.F., *Handbook of experimental fluid mechanics*, Springer, 2008.

[12] Johnstone, A., Uddin, M., Pollard, A., Calibration of hot-wire probes using non-uniform mean velocity profiles, *Expts. Fluids*, **39**, 2005, 525-532.

[13] Bailey, S.C., Kunkel, G.J., Hultmark, M., Hill, J., Meyer, K., Arnold, C.B. and Smits, Turbulence measurements using a nanoscale thermal anemometry probe. In press, *Journal of Fluid Mechanics* 2010.

[14] Shinneeb, A.-M. and Pollard, A., Investigation of vortical structures in the human airway using proper orthogonal decomposition, In preparation, 2010.

[15] Elkins, C.J., Markl, M., Pelc, N. and Eaton, J.K., 4D Magnetic resonance velocimetry for mean velocity measurements in complex turbulent flows, *Expts. Fluids*, **34**, 2003, 494-503.

[16] Seidl, V. , Muzaferija, S. and Peric, M., Parallel DNS with local grid refinement, *Applied Sci. Research*, **59**, 1998, 379-394.

[17] Karniadakis, G.E., Simulating turbulence in complex geometries, *Fluid Dynamics Research*, **24(6)**, 1999, 343-362.

[18] Hicken, J.E., Ham, F.E., Militzer, J. and Koksal, M., A shift transformation for fully conservative methods: turbulence simulation on complex, unstructured grids, *J. Comp. Physics*, **208**, 2005, 704-734.

[19] Subbareddy, P.K. and Candler, G.V., A fully discrete kinetic energy consistent finite-volume scheme for compressible flows, *J. Computational Physics*, **228(5)**, 2009, 1347-1364.

[20] Mittal, R. and Iaccarino, G., Immersed boundary methods, *Annu. Rev. Fluid Mech.*, **37**, 2005, 239-261.

[21] Roache, P.J., *Computational Fluid Dynamics*, Hermosa Publishers, Alberquerque, New Mexico, 1972.

[22] Ozem, H.L.M., *Numerical and experimental investigation of isothermal swirling flow in a flat flame burner*, Ph.D. thesis, Queen's University, 1997.

[23] Chen, S. and Doolen, G.D., Lattice Boltzmann method for fluid flows, *Annu. Rev. Fluid Mech.*, **30**, 1998, 329-364.

[24] Cockburn, B., Karniadakis, G. and Shu., C.-W., *Discontinuous Galerkin methods-theory, computation and applications*, Springer-Verlag, Heidelburg, 2000.

[25] Karniadakis, G.E. and Sherwin, S. Spectral/hp element methods for computational fluid dynamics. *Oxford Univ. Press, NY*, 2005.

[26] Bespalko, D.J., *Direct numerical simulation of turbulent channel flow using the lattice-Boltzmann Method*, M.A.Sc. Thesis, Queen's University, 2006.

[27] Bespalko, D. , Uddin, M. and Pollard, A., Addressing the anomalous pressure variance behaviour of Lattice Boltzmann method when applied to turbulent channel flow, *Submitted for publication to J. Computational Physics*, 2010.

[28] Ball, C.G., Uddin, M. and Pollard, A., Mean flow structures inside the human upper airway, *Flow, Turbulence and Combustion*, *81*, 2008, 155-188.

[29] Wei, L. and Pollard, A., Direct numerical simulation of a turbulent flow with pressure gradients, *Progress in Turbulence III, Proceedings of the 2008 iTi Conference in Turbulence Springer proceedings in Physics, Peinke, Oberlack and Talamelli (Eds.),***131**, 2010, 131-134.

[30] Wei L. and Pollard, A., Effects of Mach number and viscosity on pressure-gradient-vorticity flux correlations, em Submitted to J. Fluid Mechanics, 2010.

[31] Ball, C.G., Uddin, M. and Pollard, A., High resolution turbulence modelling of airflow in an idealised human extra-thoracic airway, *Computers & Fluids*, **37(8)**, 2008, 943-964.

[32] Agrawal, A. and Prasad, A.K., Properties of vortices in the self-similar turbulent jet, *Exp. Fluids*, **33(4)**, 2002, 565-577.

[33] Heenan, A.F., Finlay, W.H., Grgic B., Pollard, A. and Burnell, P.K.P., An investigation of the relationship between the flow field and regional deposition in realistic extra-thoracic airways, *Aerosol Science*, **35**, 2004, 1013-1023.

[34] De Backer, J.W., Vos, W.G., Verhulst, S.L., and De Backer, W., Novel imaging techniques using computer methods for the evaluation of the upper airway in patients with sleep-disordered breathing: A comprehensive review, *Sleep Medicine Reviews*, **12**, 2008, 437-447.

[35] Raiesi, H., Piomelli, U and Pollard, A., Evaluation of turbulence models using large-eddy simulation data, Accepted for publication, *ASME J. Fluids Engineering* 2010.

[36] Shinneeb, A-M and Pollard, A., Quantitative Analysis of the Flow in the Human Upper Airway Using POD, Proceedings, *15th Int Symp on Applications of Laser Techniques to Fluid Mechanics* Lisbon, Portugal, 05-08 July, 2010